

METALLICITY OF THE INTERGALACTIC MEDIUM USING PIXEL STATISTICS: IV. OXYGEN.¹

ANTHONY AGUIRRE², COREY DOW-HYGELUND², JOOP SCHAYE³, TOM THEUNS⁴

Draft version October 28, 2018

ABSTRACT

We have studied the abundance of oxygen in the IGM by analyzing O VI, C IV, Si IV, and H I pixel optical depths derived from a set of high-quality VLT and Keck spectra of 17 QSOs at $2.1 \lesssim z \lesssim 3.6$. Comparing ratios $\tau_{\text{OVI}}/\tau_{\text{CIV}}(\tau_{\text{CIV}})$ to those in realistic, synthetic spectra drawn from a hydrodynamical simulation and comparing to existing constraints on [Si/C] places strong constraints on the ultraviolet background (UVB) model using weak priors on allowed values of [Si/O]: for example, a quasar-only background yields [Si/O] ≈ 1.4 , highly inconsistent with the [Si/O] ≈ 0 expected from nucleosynthetic yields and with observations of metal-poor stars. Assuming a fiducial quasar+galaxy UVB consistent with these constraints yields a primary result that [O/C] = $0.66 \pm 0.06 \pm 0.2$; this result is sensitive to gas with overdensity $\delta \gtrsim 2$. Consistent results are obtained by similarly comparing $\tau_{\text{OVI}}/\tau_{\text{HI}}(\tau_{\text{HI}})$ and $\tau_{\text{OVI}}/\tau_{\text{SiIV}}(\tau_{\text{SiIV}})$ to simulation values, and also by directly ionization-correcting $\tau_{\text{OVI}}/\tau_{\text{HI}}$ as function of τ_{HI} into [O/H] as a function of density. Subdividing the sample reveals no evidence for evolution, but low- and high- τ_{HI} samples are inconsistent, suggesting either density-dependence of [O/C] or – more likely – prevalence of collisionally-ionized gas at high density.

Subject headings: cosmology: miscellaneous — galaxies: formation — intergalactic medium — quasars: absorption lines

1. INTRODUCTION

The enrichment of the intergalactic medium (IGM) with heavy elements has, over the past decade, become a key tool in understanding star and galaxy formation by providing a fossil record of metal formation and galactic feedback.

Absorption line spectroscopy has revealed, among other findings, that the low-density ($\delta \equiv \rho/\langle\rho\rangle \lesssim 10$) intergalactic medium (IGM), as probed by the Ly α forest and through C III, C IV, Si III, Si IV, O V, O VI, and other transitions, is at least partly enriched at all redshifts and densities probed. In particular, recent studies indicate that:

- When smoothed over large ($\sim 10 - 10^2$ kpc) scales, the abundance of carbon decreases as gas overdensity δ does and has a scatter of ~ 1 dex at fixed density. There is carbon in at least some gas at all densities down to at least the mean cosmic density, with the median carbon metallicity obeying [C/H] $\approx -3.5 + 0.65(\log \delta - 0.5)$ at $z \approx 3$ (Schaye et al. 2003, hereafter Paper II).
- On smaller ($\lesssim 1$ kpc) scales the distribution of

metals is less well known, but observations suggest that the metals may be concentrated in small, high-metallicity patches (Schaye et al. 2007).

- There is no evidence for metallicity evolution from redshift $z \approx 4$ to $z \approx 2$ (Paper II) and metals exist at some level at $z \approx 5 - 6$ (Songaila 2001; Pettini et al. 2003; Ryan-Weber et al. 2006; Simcoe 2006).

In connection with this observed widespread distribution of metals, a general picture has emerged that galactic winds – driven largely from young and/or starburst galaxies – have enriched the IGM. The same feedback may account for the dearth of low-luminosity galaxies relative to the halo mass function (e.g., Kauffmann et al. 1993; Somerville & Primack 1999; Springel & Hernquist 2003), and also for the mass-metallicity relationship of galaxies (e.g., Tremonti et al. 2004; Erb et al. 2006). However, a detailed understanding of the various feedback processes is lacking and there are still open questions and controversies concerning the time and relative importance of the various enrichment processes, and concerning the implications for galaxy formation.

Both theoretical modeling and observations of intergalactic (IG) enrichment are now advancing to the point where comparison between the two can provide crucial insight into these issues, but this comparison is not without problems. Two key difficulties concern the ionization correction required to convert observed ionic abundances into elemental abundances. First, while the oft-studied ions C IV and Si IV are observationally convenient, they are poor probes of hot ($> 10^5$ K) gas, because the ion fractions C IV/C and Si IV/Si both fall dramatically with temperature. Thus, the hot remnants of fast outflows might be largely invisible in these ions. Second, the dominant uncertainty in both the absolute and relative abundance inferences stems from uncertainty in the spectral shape of the ultraviolet ionizing background radiation

¹ Based on public data obtained from the ESP archive of observations from the UVES spectrograph at the VLT, Paranal, Chile and on data obtained at the W. M. Keck Observatory, which is operated as a scientific partnership among the California Institute of Technology, the University of California, and the National Aeronautics and Space Administration. The W. M. Keck Observatory was made possible by the generous financial support of the W. M. Keck Foundation.

² Department of Physics, University of California at Santa Cruz, 1156 High Street, Santa Cruz, CA 95064; aguirre@scipp.ucsc.edu, godelstheory@gmail.com

³ Leiden Observatory, Leiden University, P.O. Box 9513, 2300 RA Leiden, The Netherlands; schaye@strw.leidenuniv.nl

⁴ Institute for Computational Cosmology, University of Durham, South Road, Durham DH1 3LE; tom.theuns@durham.ac.uk

(UVB).

Analysis of oxygen, as probed by O VI, has the potential to shed light on both problems: this ionization state becomes prevalent in some of the very phases in which C IV and Si IV become rare, and its abundance depends on the UVB shape differently than those of other ions, helping break the degeneracy between abundances and UVB shape. The challenge posed by O VI is that at $z \gtrsim 2$ it is strongly contaminated by both Ly α and Ly β lines, making its identification and quantification difficult. Previous studies of high- z oxygen enrichment using line fitting (Carswell et al. 2002; Bergeron et al. 2002; Simcoe et al. 2004) or pixel statistics (Schaye et al. 2000a; Telfer et al. 2002; Pieri & Haehnelt 2004) have reliably detected oxygen in the IGM, and quantified its abundance in relatively dense gas, but have not assessed the oxygen abundance with a very large data sample, at very low-densities, or in a unified treatment with other available ions.

Here we extend to O VI our application of the ‘‘pixel optical depth’’ technique (e.g., Aguirre, Schaye & Theuns, hereafter Paper I) to a large set of high quality VLT/UVES and Keck/HIRES spectra. The results, when combined with previous studies of C IV and C III (Paper II) and of Si IV and Si III (Aguirre et al. 2004; hereafter Paper III), give a comprehensive observational assessment of IG enrichment by carbon, silicon and oxygen, with significantly reduced uncertainties due to the UVB shape, as well as new data on the importance of hot, collisionally ionized gas.

We have organized this paper as follows. In §§2 and 3.1 we briefly describe our sample of QSO spectra. The analysis method is described briefly in §3.1 and then in greater depth in the remainder of §3, with heavy reference to Papers I, II and III. The basic results are given in §4 and discussed in §5. Finally, we conclude in §6.

All abundances are given by number relative to hydrogen, and solar abundance are taken to be $(\text{O}/\text{H})_{\odot} = -3.13$, $(\text{C}/\text{H})_{\odot} = -3.45$, and $(\text{Si}/\text{H})_{\odot} = -4.45$ (Anders & Grevesse 1989).

2. OBSERVATIONS

We analyze 17 of the 19 high-quality (6.6 km s^{-1} velocity resolution, $\text{S}/\text{N} > 40$) absorption spectra of quasars used in Papers II and III. The two highest-redshift spectra used in those previous studies were excluded here because the severe contamination of the O VI region by H I lines makes detection of O VI nearly impossible and also introduces very large continuum fitting errors in the O VI region. Fourteen spectra were taken with the UV-Visual Echelle Spectrograph (UVES, D’Odorico et al. 2000) on the Very Large Telescope and three were taken with the High Resolution Echelle Spectrograph (HIRES, Vogt et al. 1994) on the Keck telescope. For convenience, the observed QSOs are listed in Table 1.

Regions within $\Delta v = \max(4000, 8 \text{ Mpc } H(z)/h) \text{ km s}^{-1}$ from the quasars, where $H(z)$ is the Hubble parameter at redshift z extrapolated from its present value ($H_0 \equiv 100h \text{ km s}^{-1} \text{ Mpc}^{-1}$) assuming $(\Omega_m, \Omega_{\Lambda}) = (0.3, 0.7)$, were excluded to avoid proximity effects. Regions thought to be contaminated by absorption features that are not present in our simulated spectra (e.g., damped Ly α systems) were also excluded from the analysis.

TABLE 1
OBSERVED QUASARS

QSO	z_{em}	z_{min}	z_{max}	λ_{min} (Å)	instrument	ref	Err
Q1101-264	2.145	1.878	2.103	3050.00	UVES	1	1.6
Q0122-380	2.190	1.920	2.147	3062.00	UVES	2	0.6
J2233-606	2.238	1.963	2.195	3055.00	UVES	3	1.1
HE1122-1648	2.400	2.112	2.355	3055.00	UVES	1	1.4
Q0109-3518	2.406	2.117	2.361	3050.00	UVES	2	1.5
HE2217-2818	2.406	2.117	2.361	3050.00	UVES	3	1.6
Q0329-385	2.423	2.133	2.377	3062.00	UVES	2	1.2
HE1347-2457	2.534	2.234	2.487	3050.00	UVES	1,2	2.5
PKS0329-255	2.685	2.373	2.636	3150.00	UVES	2	1.5
Q0002-422	2.76	2.441	2.710	3055.00	UVES	2	1.6
HE2347-4342	2.90	2.569	2.848	3428.00	UVES	2	1.5
Q1107+485	3.00	2.661	2.947	3644.36	HIRES	4	2.3
Q0420-388	3.123	2.774	3.068	3760.00	UVES	2	1.8
Q1425+604	3.20	2.844	3.144	3736.20	HIRES	4	2.1
Q2126-158	3.268	2.906	3.211	3400.00	UVES	2	2.0
Q1422+230	3.62	3.225	3.552	3645.24	HIRES	4	3.1
Q0055-269	3.655	3.257	3.586	3423.00	UVES	1	4.0

REFERENCES. — (1) Kim et al. 2002; (2) Kim et al. 2004; (3) Kim, Cristiani, & D’Odorico 2001; (4) Rauch et al. 1997.

NOTE. — Columns 1 and 2 contain the quasar name and corresponding Ly α emission redshift. Columns 3 and 4 contain the minimum and maximum absorption redshifts considered and Column 5 contains the corresponding minimum observed wavelength. The last column contains an estimate of the percentage uncertainty in the continuum fitting in the O VI region.

Lyman continuum contamination increases significantly towards lower wavelengths, whereas (as described below) our correction for this contamination assumes that it is non-evolving. To mitigate this effect, only the red portion [$\geq \text{med}(z)$] of the QSO spectra used in Papers II and III is analyzed in this Paper. As in Schaye et al. (2000a), this was found to result in smaller errors than using the full region.

Further details concerning the sample and data reduction are given in Paper II (§2).

3. METHOD

The pixel optical depth method we use for measuring O VI is similar to that described in Papers I, II, and III. Section 3.1 contains a brief outline of the method; §3.2 and §3.3 describe continuum fitting and contamination corrections, which have been changed slightly from the methods described in Papers II and III; §3.4 describes tests of the recovery, and §3.5 discusses the ionization balance of the relevant species, and describes how ionization corrections are performed.

3.1. Overview

The basic method for analysis of each QSO spectrum is as follows:

1. Optical depths due to H I Ly α ($\lambda 1216 \text{ \AA}$) absorption are recovered for all pixels in the Ly α forest region, using higher-order Lyman lines to estimate optical depths for saturated pixels.
2. The pixel optical depth at the corresponding wavelengths of the metal lines O VI ($\lambda\lambda 1032, 1038$), C IV ($\lambda\lambda 1548, 1551$), and Si IV ($\lambda\lambda 1394, 1403$) are recovered, making several corrections to reduce contamination and noise.

3. The recovered optical depth in one transition is compared with that of another, by binning the pixels in terms of the optical depth of H I, C IV, or Si IV, and plotting the median (or some other percentile of) optical depth of O VI. A correlation then indicates a detection of O VI absorption. An example is shown in Fig. 1.

As was done in Papers II and III, an identical analysis is applied to synthetic spectra generated using a cosmological, hydrodynamical simulation, kindly provided by Tom Theuns. For each observed quasar we generate 50 corresponding simulated spectra with the same noise properties, wavelength coverage, instrumental broadening, and pixel size as the observed spectra. For each UVB model (of which several are used; see below) the carbon distribution as measured in Paper II, and the value of [Si/C] from Paper III, are imposed on the fiducial spectra. An oxygen abundance is assigned by assuming a *constant, uniform* value of [O/C]. Ionization balances are calculated using CLOUDY⁵ (version 94; see Ferland et al. 1998 and Ferland 2000 for details). A direct comparison of the results from these simulated and observed spectra allows for inferences about the distribution of oxygen, carbon, and silicon. The same simulation was used in Papers I (§3), II, and III, to which the reader is referred for details.

This study employs the identical UVB models used in Papers II (§4.2) and III, excluding model “QGS3.2”. All models are from Haardt & Madau (2001, hereafter HM01)⁶. These have been renormalized (by a redshift-dependent factor) such that the simulated spectra match the observed evolution of the mean H I Ly α absorption (Paper II). The fiducial model, “QG”, includes contributions from both galaxies (with a 10% escape fraction for ionizing photons) and quasars; “Q” includes only quasars; “QGS” is an artificially softened version of QG: its flux has been reduced by a factor of ten above 4 Ryd. The UVB used in the simulation only affects the IGM temperature, and was chosen to match the measurements by Schaye et al. (2000b).

3.2. Continuum fitting

A major source of error in O VI optical depths is continuum fitting in the O VI absorption region, where contamination by Ly α and Ly β lines is heavy. To make this fitting as accurate as possible, and to furnish an estimate of the continuum fitting error, we have applied the following procedure to the region analyzed for O VI absorption (in the case of observed spectra, this was done after the spectra had been continuum fitted by eye as described in Paper II §2):

1. The spectral region is divided into 20 Å (rest-frame) segments.
2. In segments with large unabsorbed regions, an automatic continuum fitting algorithm is applied (see §5.1 of Paper II), in which pixels $> 1\sigma$ below the continuum are iteratively removed.

⁵ See <http://www.pa.uky.edu/~gary/cloudy>.

⁶ The data and a description of the input parameters can be found at <http://pitto.mib.infn.it/~haardt/refmodel.html>.

3. In segments without large unabsorbed regions, we identify small unabsorbed regions or regions absorbed only in Ly β ; the latter are identified by superimposing the region of the spectrum corresponding to Ly α absorption. The continuum level of the segment is fit by minimizing the deviation of identified unabsorbed regions from unit flux, and deviation of the Ly β regions from the corresponding scaled Ly α features.

4. A spline is interpolated between the fits to all segments and the spectrum is rescaled by this spline.

This procedure was applied to all observed spectra as well as to one simulated spectrum per observed spectrum, where a 10-20% error in the continuum was introduced on scales of 1, 4 and 16 segments. The median absolute errors remaining after blindly fitting the continua of the simulated spectra are given in Table 1 as an estimate of continuum fitting errors in the corresponding observed spectra. Because the procedure is not fully automatic, we were unable to apply it to all of the simulated spectra.

The region redwards of Ly α was fit in both simulated and observed spectra using the procedure described in §5.1 step I of Paper II. Continuum fitting errors are much smaller for this region ($\sim 0.01\%$).

3.3. Correcting for contamination

After continuum fitting the spectra, H I (Ly α) optical depths τ_{HI} are derived for each pixel between the quasar’s Ly α and Ly β emission wavelengths, save for regions close to the quasar to avoid proximity effects (see §2). If Ly α is saturated (i.e., $F(\lambda) < 3\sigma(\lambda)$, where F and σ are the flux and noise arrays, see Paper I, §4.1; Paper II, §5.1, step 2), higher-order Lyman lines are used to estimate τ_{HI} .

Corresponding O VI, Si IV, and C IV optical depths (τ_{OVI} , τ_{SiIV} , τ_{CIV}) are subsequently derived for each H I pixel. We exclude regions of the quasar spectrum that are contaminated by absorption features that are not included in our simulated spectra, such as Ly α lines with damping wings. For τ_{SiIV} and τ_{CIV} , corrections are made for self-contamination and contamination by other metal lines, as described in Paper I, §4.2.

As shown in Fig. 1, when plotting each percentile in τ_{OVI} absorption against absorption in some other ion, the correlation disappears below some O VI optical depth τ_{min} (corresponding to a value τ_c in the other ion) that is determined by noise, continuum fitting errors, and contamination by other lines. These effects may then be corrected for by subtracting τ_{min} from the binned optical depths, thus converting most points below τ_c into upper limits. For each realization and for each percentile, we compute τ_{min} as the given percentile of optical depth for the set of pixels with optical depth $< \tau_c$. We use values $\tau_c = 0.01$ when binning in C IV or Si IV, and of $\tau_c = 0.1$ when binning in H I, as we never see a correlation extending below these values.⁷

The error on τ_{min} for an individual realization is computed by dividing the spectrum into 5 Å segments, then bootstrap-resampling the spectrum by choosing these

⁷ In Paper II we used functional fits to determine τ_c . For OVI the correlations are generally less strong than for CIV and we fix τ_c “by hand.”

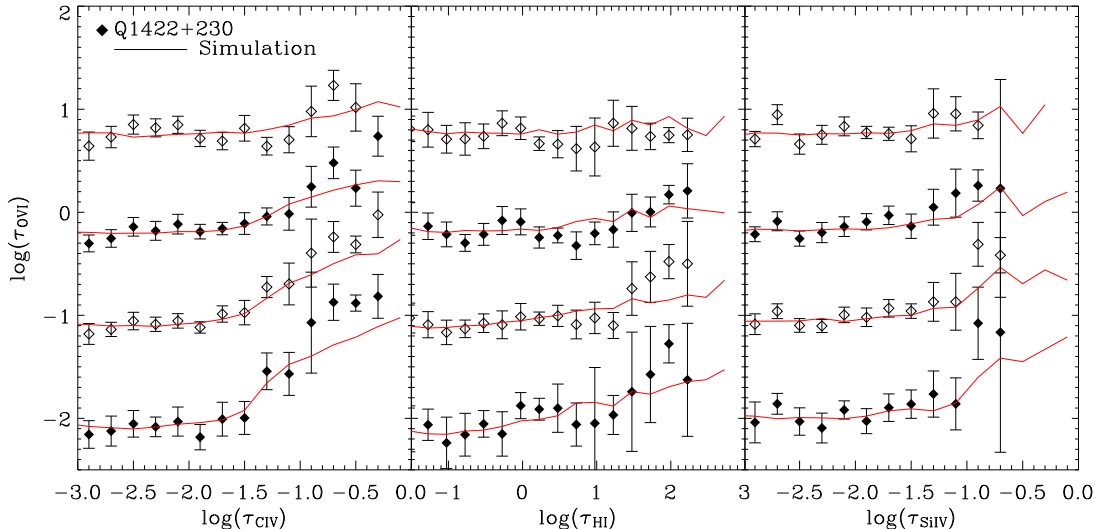


FIG. 1.— O VI optical depths as a function of τ_{CIV} (left), τ_{HI} (middle), and τ_{SiIV} (right). From bottom to top, the points represent the 31st, median, 69th, and 84th percentiles. Data points are plotted with 1σ error bars. The red lines are predictions from simulations with $\langle [\text{C}/\text{H}] \rangle = -3.8 + 0.65\delta$, $\sigma = 0.70$, $[\text{Si}/\text{C}] = 0.77$, $[\text{O}/\text{C}] = 0.64$. The observed and simulated 31st, 69th and 84th percentiles have been offset vertically by -0.5 , 0.5 and 1.0 dex, respectively.

chunks with replacement, and finally computing the variance of τ_{min} as computed from 100 such resampled spectra. When the realizations are combined, τ_{min} is instead computed as the median among the realizations, and the error on this value is computed by bootstrap-resampling the realizations. For further details see Paper II, §5.1, step 4 and Paper III, §3.4.

As noted above, Ly α and higher Lyman transitions heavily contaminate the O VI absorption regime. This can add substantial error in the recovered τ_{OVI} . Two corrections are made to minimize this contamination. First, after recovering τ_{HI} and τ_{OVI} , an initial correction is made for contamination by higher-order H I lines by subtracting

$$\tau_{\text{corr}}(\lambda) = \tau_{\text{Ly}\alpha}(\lambda') (f_{\text{Ly}i} \lambda_{\text{Ly}i} / f_{\text{Ly}\alpha} \lambda_{\text{Ly}\alpha}), \quad (1)$$

where f is the transition oscillator strength, $\lambda' = (\lambda_{\text{Ly}\alpha} / \lambda_{\text{Ly}i}) \lambda$ is the redshifted Lyman α wavelength corresponding to Ly i absorption observed at wavelength λ and i corresponds to first five higher order Lyman lines (i.e., Ly β λ 1025 through Ly ζ λ 930).

A second correction is made by taking the minimum of the O VI doublet,

$$\tau_{\text{OVI}} = \min \left(\tau_{\text{OVIa}}, \frac{f_{\text{OVIa}} \lambda_{\text{OVIa}} \tau_{\text{OVIb}}}{f_{\text{OVIb}} \lambda_{\text{OVIb}}} \right) \quad (2)$$

where ‘a’ and ‘b’ denote the stronger and weaker doublet components, respectively. These corrections are described in detail in Paper I, §4.2.

Another potential contamination issue is that due to strong Ly α or Ly β absorption, some higher percentiles in O VI absorption can become dominated by saturated pixels, so that the particular value of the percentile is determined by the contaminating lines rather than by the O VI distribution. To remove these unreliable percentiles from consideration, the average noise $\bar{\sigma}_{\text{sat}}$ is calculated for saturated O VI pixels and is converted into a maximum optical depth ($\tau_{\text{sat}} = -\ln 3\bar{\sigma}_{\text{sat}}$). After O VI optical depths

are binned, those percentile bins with $\tau_{\text{OVI}} > \tau_{\text{sat}}$ are excluded from the analysis.

3.4. Testing O VI Recovery

Because there is substantial processing of the recovered O VI optical depths, it is important to test how efficiently the true O VI optical depths are recovered by our procedures. To do so, simulations were produced just as described in § 3.1, but with (effectively) perfect resolution, no noise, and only O VI λ 1032 absorption (and hence no contamination or self-contamination). In Fig. 2 the recovered O VI pixel optical depths are plotted against these “true” optical depths for a set of 60 simulated spectra, for two representative QSOs (see Paper I for more such tests). Of particular note is the efficacy of subtracting the “flat level” τ_{min} as described in the preceding section. Ideally, τ_{min} would be determined using pixels with negligible O VI absorption; this is possible in the present case (as the true O VI optical depths are known) and corresponding results are shown in the left panels. In a realistic case, a proxy for O VI must be used; in the right panels of Fig. 2, H I is employed and τ_{min} is computed using all pixels with $\log \tau_{\text{HI}} < -1$. In both cases, the subtracted τ_{min} values are shown as horizontal dashes on the right axes of Fig. 2.

Overall, we find that using τ_{HI} to calculate τ_{min} is effective at recovering $\tau_{\text{OVI}} > 10^{-2.5}$ for the 31st and median percentiles; for higher percentiles the recovery is accurate only at higher τ_{OVI} , but the large ‘scatter’ indicates that this is random, rather than systematic error.

3.5. Ionization corrections

In Papers I and II it was shown from simulations that there exists a tight correlation between τ_{HI} and the absorbing gas density and temperature, which could be used to predict an ionization correction (i.e., the ratios of O VI/O and H I/H) as a function of density; for details

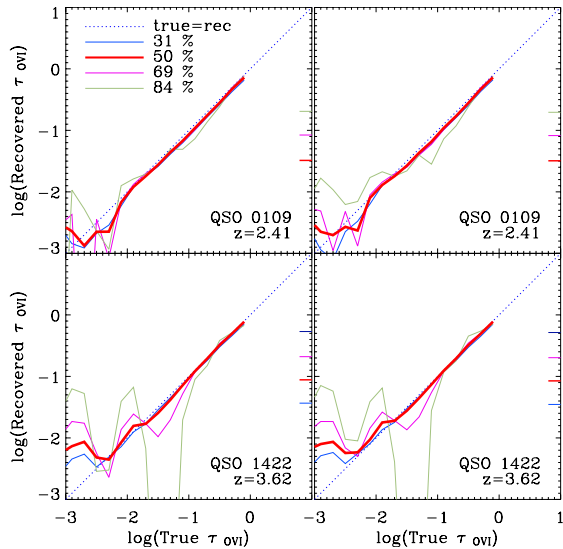


FIG. 2.— The accuracy of recovering the “true” OVI pixel optical depth from simulated spectra of Q0109–3518 and Q1422+230. For every panel, the recovered OVI optical depth is plotted against the “true” optical depth, τ_{true} . Each panel shows the binned percentiles after τ_{min} has been subtracted from the recovered τ_{OVI} pertaining to that percentile. The left and right panels calculate τ_{min} using the $\log \tau_{\text{true}} < -3$ and $\log \tau_{\text{HI}} < -1$ respectively. These are shown as horizontal dashes on the right axis of each plot. For $\log \tau_{\text{OVI}} > -2$ the median OVI optical depths are effectively recovered.

see § 6 in Paper I and § 5.1 in Paper II. As noted in Papers II and III, this works well for C IV and less well for Si IV, due to their mild and strong ionization correction dependence on τ_{HI} , respectively.

In the upper panel of Figure 3 we provide a contour plot of the logarithm of the predicted fraction of O VI ions versus temperature and density. The middle and lower panels show $\log \tau_{\text{OVI}}/\tau_{\text{CIV}}$ for $[\text{O}/\text{C}]=0$, and $\log \tau_{\text{OVI}}/\tau_{\text{HI}}$ for $[\text{O}/\text{H}]=0$, respectively. For photoionized gas ($T \lesssim 10^5 \text{ K}$) the O VI fraction is highest for $-5 \lesssim \log n_{\text{H}} \lesssim -4$, and only weakly dependent on the temperature.

However, for higher densities (and $T \lesssim 10^5 \text{ K}$), the O VI fraction falls quickly, resulting in a very large ionization correction for H I saturated pixels. At the same time, the O VI fraction at high density increases with T for $T \gtrsim 10^5 \text{ K}$, so that collisionally ionized gas might be detected relatively easily. Therefore at high τ_{HI} , collisionally ionized O VI gas can easily swamp photoionized O VI. This can be seen most clearly in the bottom panel, which shows that for fixed $[\text{O}/\text{H}]$ and density, $\tau_{\text{OVI}}/\tau_{\text{HI}}$ increases quickly at $T \gtrsim 10^5 \text{ K}$, particularly if the density is high. Because our $\tau_{\text{HI}} - \rho$ relation is dominated by photoionized gas (with $T < 10^5$), the effects of collisionally ionized gas are potentially important and are discussed at length in § 5.4 below.

The strategy employed here is to employ our fiducial ionization corrections as in Papers II and III, but to recognize that at high-density, the results may be significantly affected by collisionally ionized gas. It is important to note that the importance of collisionally ionized gas may be underestimated by our simulation, because we did not include a mechanism for generating galactic winds, which could shock-heat the gas surrounding

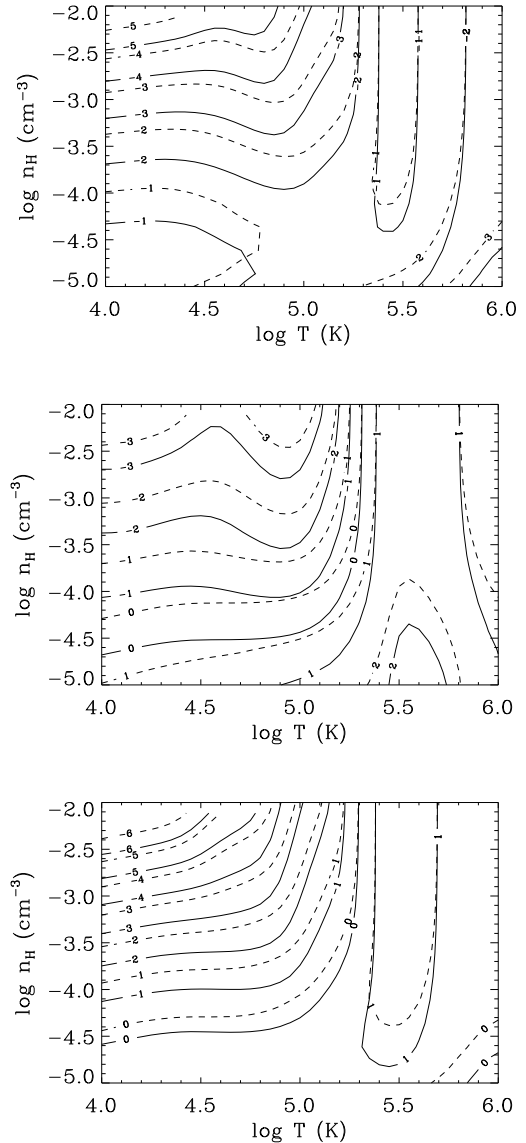


FIG. 3.— OVI ion fraction $N_{\text{OVI}}/N_{\text{O}}$ (top), $\log \tau_{\text{OVI}}/\tau_{\text{CIV}}$ for $[\text{O}/\text{C}]=0$ (middle), and $\log \tau_{\text{OVI}}/\tau_{\text{HI}}$ for $[\text{O}/\text{H}]=0$ (bottom) as functions of temperature and the hydrogen number density. Solid (dashed) contours are for the $z = 3$ UV background model QG (Q). A measurable quantity of OVI could be collisionally ionized if $T \gtrsim 10^5 \text{ K}$, which would be misinterpreted as photoionized gas during the ionization correction process. This gas would potentially contain very little associated CIV and HI.

galaxies. Our simulation does, however, include heating by gravitational accretion shocks.

Once the ionization correction has been determined, and corrected O VI optical depths and recovered H I optical depths τ_{HI} have been obtained, the oxygen abundance can be calculated:

$$[\text{O}/\text{H}] = \log \left(\frac{\tau_{\text{OVI}} (f\lambda)_{\text{HI}} n_{\text{O}} n_{\text{HI}}}{\tau_{\text{HI}} (f\lambda)_{\text{OVI}} n_{\text{OVI}} n_{\text{H}}} \right) - (\text{O}/\text{H})_{\odot}, \quad (3)$$

where f_i and λ_i are the oscillator strength and rest wavelength of transition i , respectively ($f_{\text{OVI}} = 0.1329$, $f_{\text{HI}} = 0.4164$, $\lambda_{\text{OVI}} = 1031.9270 \text{ \AA}$, $\lambda_{\text{HI}} = 1215.6701 \text{ \AA}$), and we use the solar abundance $(\text{O}/\text{H})_{\odot} = -3.13$ (num-

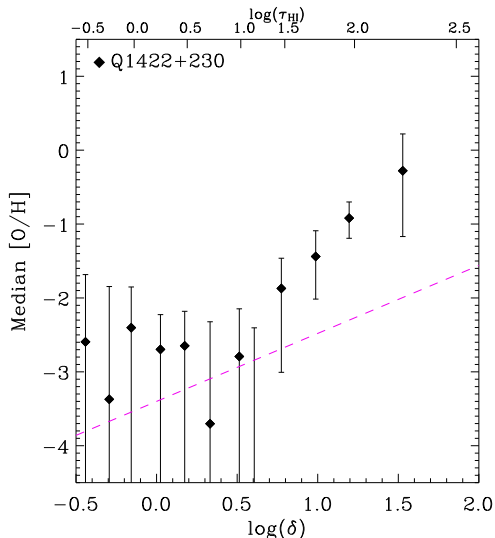


FIG. 4.— The median oxygen abundance as a function of the overdensity (*bottom axis*) or τ_{HI} (*top axis*), by applying the ionization correction of §3.5 and Paper II. For reference, the dashed line is $[\text{O}/\text{H}]$ vs. density, assuming the carbon distribution fit for Q1422+230 from Paper II and constant $[\text{O}/\text{C}]=0.64$.

ber density relative to hydrogen; Anders & Grevesse 1989). An example of the results from this analysis applied to the observed spectrum of Q1422+230 is shown in Figure 4.

In Figure 5 we show a test in which we have generated simulated spectra using the “QG” ionizing background, recovered optical depths, and applied the just-described ionization correction to recover the oxygen abundance. The true metallicity is given by the carbon distribution of Paper II (for the QG background), with a fixed $[\text{O}/\text{C}]=\log 4.5 \approx 0.65$ (i.e., $[\text{O}/\text{H}]=-3.15+0.65\delta$), and is shown on the plot as a dashed line. For $\log \delta \leq 1.5$, the O VI abundance recovery is promising: it overestimates by less than 0.3 dex, and the dependence of δ is reproduced. However, the overestimation appears to increase for $\log \delta \geq 1.5$, reaching approximately 1 dex for the highest overdensity bin. The difference in the high-versus low- δ gas can probably be attributed to the collisionally ionized gas residing in and around dense regions, due to gravitational accretion shocks. We should thus keep in mind that we expect to overestimate the oxygen abundance associated with strong H I absorbers.

4. RESULTS

Our basic result will be an estimate of $[\text{O}/\text{C}]$ for the low-density IGM as a whole, computed using four different but consistent methods, which we describe in turn.

4.1. τ_{OVI} versus τ_{CIV} for the full sample

To extract as much information as possible from our data we have, as in papers II and III, combined the data points obtained from our entire sample. Figure 6 shows $\log \tau_{\text{OVI}}/\tau_{\text{CIV}}$ versus $\log \tau_{\text{CIV}}$, in bins of z . To generate these points, we begin with τ_{OVI} values binned in τ_{CIV} for each QSO, as in Fig. 1 for Q1422+230. We then subtract from each the “flat level” τ_{min} for that QSO to adjust for noise, contamination, etc. (see § 3.1), then divide by the central value of the τ_{CIV} bin. These points,

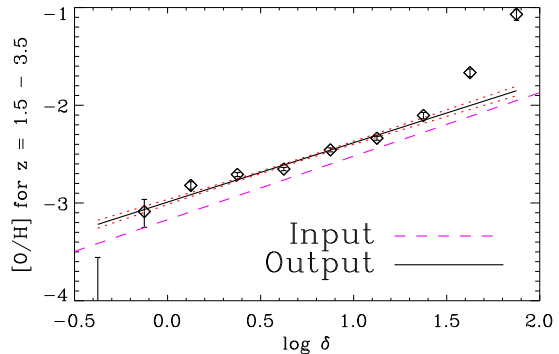


FIG. 5.— Test of the OVI ionization correction from the synthetic spectra using the full QSO sample (using 50 realizations of each synthetic spectrum so as to focus on systematic effects). The input line represents the OVI distribution imposed on the simulations, and the output line is that recovered from the analysis and ionization correction, fit to the data at $\log \delta \leq 1.5$; in this density range, the recovery is accurate to within 0.3 dex.

gathered from all QSOs, are rebinned by determining, for each τ_{CIV} bin in Fig. 6, the best constant-level χ^2 -fit to all of the points in the specified redshift bin. The errors represent 1- and 2- σ confidence intervals ($\Delta\chi^2 = 2$ and $\Delta\chi^2 = 4$) on this fit.

The plotted lines indicate corresponding optical depths from synthetic spectra drawn from the simulation, using several UVB models, the corresponding $[\text{C}/\text{H}]$ distributions as determined in Paper II, and a constant $[\text{O}/\text{C}]$ value determined as follows. For each background, we generate simulated $\tau_{\text{OVI}}/\tau_{\text{CIV}}$ points in the same way as we did for the observations, but averaging over 50 simulated realizations as described in § 3.1. We then calculate a χ^2 between all valid observed original (not rebinned) points and the corresponding simulated points.⁸ Because we use 50 simulated realizations, the simulation errors are almost always negligible compared to the observed errors, but they are still taken into account by calculating the total χ^2 using the formula:

$$\chi^2 = \sum_i \left[\left(\frac{X_{\text{obs}} - X_{\text{sim}}}{\sigma_{\text{obs}}} \right)^{-2} + \left(\frac{X_{\text{obs}} - X_{\text{sim}}}{\sigma_{\text{sim}}} \right)^{-2} \right]^{-1}, \quad (4)$$

where $X \equiv \tau_{\text{OVI}}/\tau_{\text{CIV}}$ and σ is the error in this quantity. We then add a constant offset to the simulated points (which corresponds to scaling $[\text{O}/\text{C}]$) such that χ^2 is minimized. In each panel the lines connect the scaled, rebinned simulation points.

The first evident result is that $\log \tau_{\text{OVI}}/\tau_{\text{CIV}} \sim 0$ and appears to be at most weakly dependent on $\log \tau_{\text{CIV}}$, from $\log \tau_{\text{CIV}} = -1.5$ to 0. This is unlike τ_{SIV} , which increases by ≈ 2 dex in this τ_{CIV} regime (Paper II). At the lowest densities the data exhibits a decline. Comparing these panels suggest there is little dependence on redshift in this interval. This can be seen more clearly in Figure 7, which show $\log \tau_{\text{OVI}}/\tau_{\text{CIV}}$ versus z in bins of τ_{CIV} : there is no evidence, in either the simulated or ob-

⁸ Even using 50 realizations, it may occasionally happen that a simulated bin fails to have enough pixels for at least five realizations, and so is undefined; in this case the observed point is discarded as well.

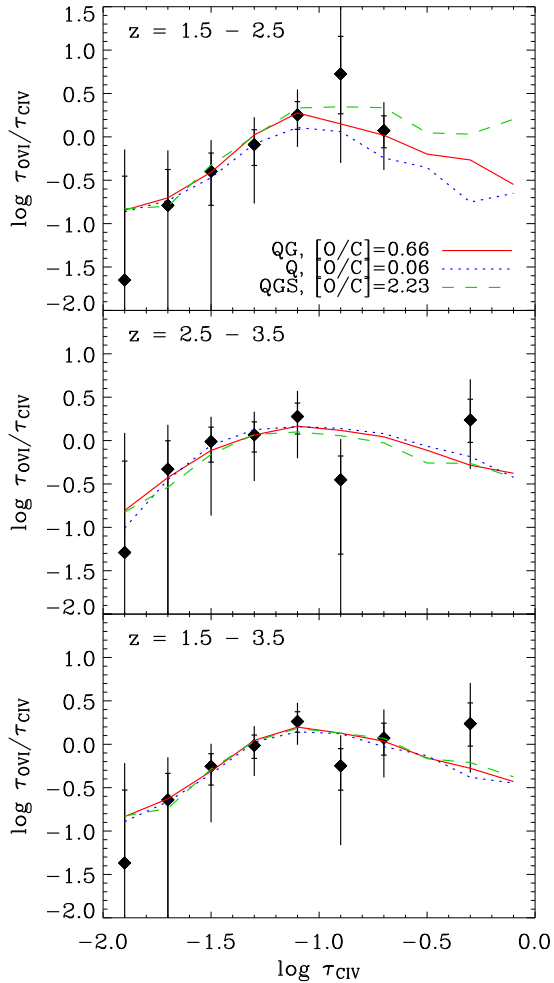


FIG. 6.— Rebinned median $\log(\tau_{\text{OVI}}/\tau_{\text{CIV}})$ vs. $\log \tau_{\text{CIV}}$ in bins of z for the combined QSO sample. The first two panels show bins centered at $z = 2$ and 3 with width $\Delta z = 1$; the bottom panel shows combined data for all redshifts. Data points are plotted with 1 and 2σ error bars. The lines represent corresponding simulation points (with errors suppressed and with $[\text{O}/\text{C}]$ chosen to minimize the χ^2) using different UVB models, as indicated in the legend of the top panel.

served points, for evolution in $\tau_{\text{OVI}}/\tau_{\text{CIV}}$ for $1.5 \leq z \leq 3.5$.

The observed trends in $\log(\tau_{\text{OVI}}/\tau_{\text{CIV}})$ are reproduced well by the simulations. Therefore, because $\tau_{\text{OVI}}/\tau_{\text{CIV}}$ scales with $[\text{O}/\text{C}]$, the offset in $\tau_{\text{OVI}}/\tau_{\text{CIV}}$ obtained by minimizing the χ^2 (Eq. 4) against the observations can be used to reliably compute the best fit $[\text{O}/\text{C}]$. As an example, for our fiducial UVB model QG, the simulated spectra were generated with $[\text{O}/\text{C}] = 0.65$ and best fit by an offset of $+0.01$ dex (implying a best-fit $[\text{O}/\text{C}] = 0.66$), with $\chi^2/\text{d.o.f.} = 42.7/82$. As we found in Paper II and for Q1422+230 above, the reduced χ^2 is somewhat low. This is due to a slight overestimate of the errors at low- τ_{CIV} (Paper II) and to the fact that the data points are not completely independent (because single absorbers contribute to multiple data points).

The fitted $[\text{O}/\text{C}]$ values and corresponding $\chi^2/\text{d.o.f.}$, are listed in Table 2, with errors computed by bootstrap-resampling the quasars used in the χ^2 minimization. For

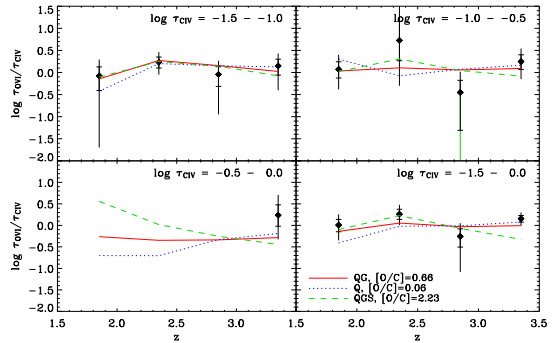


FIG. 7.— Rebinned median $\log(\tau_{\text{OVI}}/\tau_{\text{CIV}})$ vs. z in cuts of τ_{CIV} for the combined QSO sample. Data points are plotted with 1 and 2σ error bars, where green lines denote lower error of $-\infty$. The first three panels show bins centered at $\log \tau_{\text{CIV}} = -1.25, -0.75$ and -0.25 with width 0.5 , dex; the bottom-right panel shows data for all τ_{CIV} combined. The lines are the same as in Fig. 6.

our fiducial model, QG, the best fit $[\text{O}/\text{C}] = 0.66^{+0.06}_{-0.06}$. The quasar-only background Q (which is probably too hard; see Paper II) gives a much lower value of $[\text{O}/\text{C}] = 0.06^{+0.06}_{-0.06}$. The softer QGS backgrounds gives implausibly high values of $[\text{O}/\text{C}] = 2.23^{+0.06}_{-0.06}$. Coupling this with results from Paper II suggesting that the QGS background is unrealistically soft, strongly disfavors this UVB model.

We may also subdivide our sample by redshift to test the dependence of $[\text{O}/\text{C}]$ on these. First, computing $[\text{O}/\text{C}]$ using only spectra that have a median absorption redshift $\text{med}(z) > 2.5$ (see Table 1) yields $[\text{O}/\text{C}] = 0.71 \pm 0.07$, versus $[\text{O}/\text{C}] = 0.58 \pm 0.10$ using the spectra with $\text{med}(z) < 2.5$; these are consistent to about 1σ . Using the Q and QGS UVBs, the $[\text{O}/\text{C}]$ values inferred from the redshift subsamples are marginally consistent with each other and with the full sample.

4.2. τ_{OVI} versus τ_{HI} for the full sample

While the $\tau_{\text{OVI}}/\tau_{\text{CIV}}$ ratios give the most direct constraints on $[\text{O}/\text{C}]$, it is also useful to examine $\tau_{\text{OVI}}/\tau_{\text{HI}}$, since comparing the simulated to the observed $\tau_{\text{OVI}}/\tau_{\text{HI}}$ ratios gives an additional (but related) estimate of $[\text{O}/\text{C}]$ (recall that our simulation reproduces the observed $\tau_{\text{CIV}}(\tau_{\text{HI}})$).

Figure 8 shows $\log \tau_{\text{OVI}}/\tau_{\text{HI}}$ versus τ_{HI} for our combined sample, in bins of redshift. Lines again connect the simulation points (with an overall scaling to best match the observations), which reproduce the observed trends in z and τ_{HI} . The scalings correspond to best-fit $[\text{O}/\text{C}]$ of 0.69 ± 0.06 , 0.19 ± 0.06 , and 2.25 ± 0.06 , for QG, Q, and QGS, respectively. For QG and QGS, the inferred $[\text{O}/\text{C}]$ are consistent with the results found using $\tau_{\text{OVI}}/\tau_{\text{CIV}}$; for our hardest UVB model, Q, the $[\text{O}/\text{C}]$ values are more discrepant, but still within 1.5σ .

However, while the simulations reproduce the overall trends present in the data, there are some possible discrepancies. Although the $\log \tau_{\text{HI}} \leq 0.3$ points are upper limits, the simulations also appear to fall marginally above the data in this regime. At $\log \tau_{\text{HI}} \gtrsim 1$, on the other hand, the simulations slightly but significantly underpredict τ_{OVI} . This can be seen more clearly in Figure 9, where $\log \tau_{\text{OVI}}/\tau_{\text{HI}}$ versus z in bins of τ_{HI} is shown, exhibiting a clear discrepancy for points at high- z and

TABLE 2
 BEST-FIT ABUNDANCES

UVB model	[O/C] ^a	$\chi^2/\text{d.o.f.}$	[O/C] ^b	[Si/C]	$\chi^2/\text{d.o.f.}$	[Si/O]	[C/H]= $\alpha+\beta(z-3)+\gamma(\log \delta - 0.5)$			
							α	β	γ	$\chi^2/\text{d.o.f.}$
QG	0.66 ± 0.06	42.7/82	0.56 ± 0.08	0.77 ± 0.05	65.7/115	0.11 ± 0.08	$-3.47^{+0.07}_{-0.06}$	$0.08^{+0.09}_{-0.06}$	$0.65^{+0.10}_{-0.14}$	114.1/184
Q	0.06 ± 0.06	59.9/82	0.06 ± 0.08	$1.48^{+0.05}_{-0.06}$	65.6/115	1.42 ± 0.08	-2.91 ± 0.07	-0.06 ± 0.09	0.17 ± 0.08	113.8/184
QGS	2.23 ± 0.06	26.7/82	2.11 ± 0.09	$0.26^{+0.06}_{-0.07}$	73.8/115	-1.97 ± 0.11	$-4.14^{+0.06}_{-0.05}$	$0.54^{+0.10}_{-0.07}$	1.31 ± 0.07	114.2/184

NOTE. — The best-fit abundances and corresponding χ^2/dof from this work, and Papers II ([C/H]) and III ([Si/C]). Errors were computed by bootstrap-resampling the quasars used in the χ^2 minimization.

^aComputed using $\tau_{\text{OVI}}/\tau_{\text{CIV}}$ vs. τ_{CIV} ; see § 4.1.

^bComputed using $\tau_{\text{OVI}}/\tau_{\text{HI}}$ vs. τ_{HI} for gas of density $\delta \leq 10$; see § 4.2.

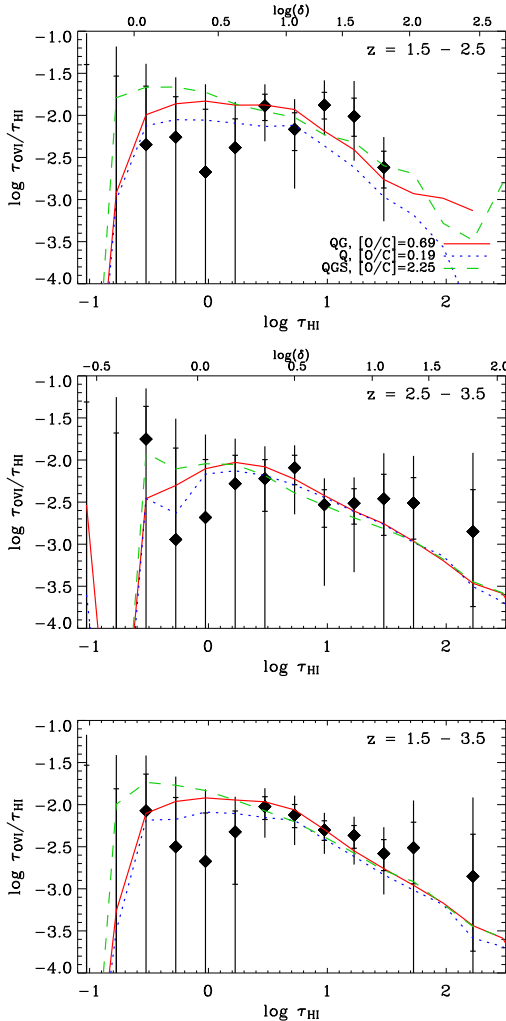


FIG. 8.— Rebinned median $\log \tau_{\text{OVI}}/\tau_{\text{HI}}$ vs. $\log \tau_{\text{HI}}$ in bins of z for the combined QSO sample. The top two panels show bins centered at $z = 2$ and 3 with width $\Delta z = 1$; the bottom panel shows combined data for all redshifts. Data points are plotted with 1σ and 2σ error bars. The lines represent corresponding simulation points (with errors suppressed and with [O/C] chosen to minimize the χ^2) using different UVB models, as indicated in the legend in the top panel.

high τ_{HI} . Indeed, if we consider subsamples above and below $\log \tau_{\text{HI}} = 1$, we find that for $\log \tau_{\text{HI}} < 1$ we obtain

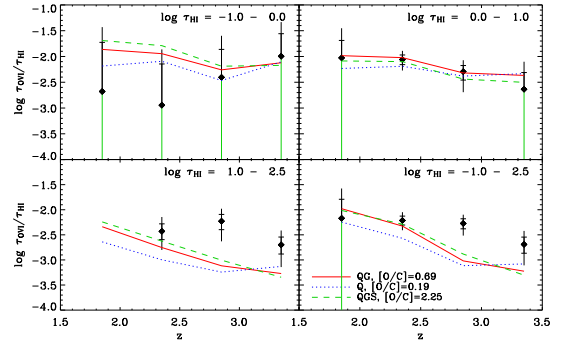


FIG. 9.— Rebinned median $\log(\tau_{\text{OVI}}/\tau_{\text{HI}})$ vs. z in cuts of τ_{HI} for the combined QSO sample. Data points are plotted with 1 and 2σ error bars, where green lines denote lower error of $-\infty$. The top two panels show bins centered at $\log \tau_{\text{HI}} = -0.50$ and 0.50 with width 1.0 dex; the bottom-left panel corresponds to a bin centered at $\log \tau_{\text{CIV}} = 1.75$ with width 1.50 dex; the bottom-right panel shows data for all τ_{CIV} combined. The lines are the same as in Fig. 8

[O/C] values consistent those obtained from $\tau_{\text{OVI}}/\tau_{\text{CIV}}$ (0.62 ± 0.07 , 0.13 ± 0.07 and 2.18 ± 0.07 for QG, Q, and QGS respectively), but for $\log \tau_{\text{HI}} > 1$ we obtain [O/C] of 0.92 ± 0.10 , 0.34 ± 0.10 , and 2.52 ± 0.11 for QG, Q, and QGS respectively. This discrepancy in [O/C] for between low- and high- τ_{HI} subsamples is significant at $\approx 2.5\sigma$ for the QG and QGS models, and at 1.7σ for the Q model.

Given the tight (but z -dependent) relation between τ_{HI} and gas density (see Paper II, Fig. 2, and the upper axis in the top two panels of Fig. 8), it is useful also to divide our sample into high- and low-density subsamples. We have done this by recomputing [O/C] from $\tau_{\text{OVI}}/\tau_{\text{HI}}$ using only bins with τ_{HI} corresponding to $\delta < 10$ or $\delta > 10$. For $\delta < 10$, we obtain [O/C] of 0.56 ± 0.08 , 0.06 ± 0.08 , and 2.11 ± 0.09 (all consistent at 1σ with the full sample), whereas for $\delta > 10$ we obtain [O/C] of 1.02 ± 0.09 , 0.51 ± 0.09 , and 2.60 ± 0.09 for QG, Q, and QGS, respectively (all discrepant at $\approx 4\sigma$).

This high- δ and (less significantly) high- τ_{HI} difference might have several causes. First, it might correspond to a genuine change in [O/C] with gas density. In this case, however, such an effect would also be expected in the trends of $\tau_{\text{OVI}}/\tau_{\text{CIV}}$ vs. τ_{CIV} – and no such effect is evident. Thus, we consider it more likely that there exists a significant portion of hot gas – not present in the simu-

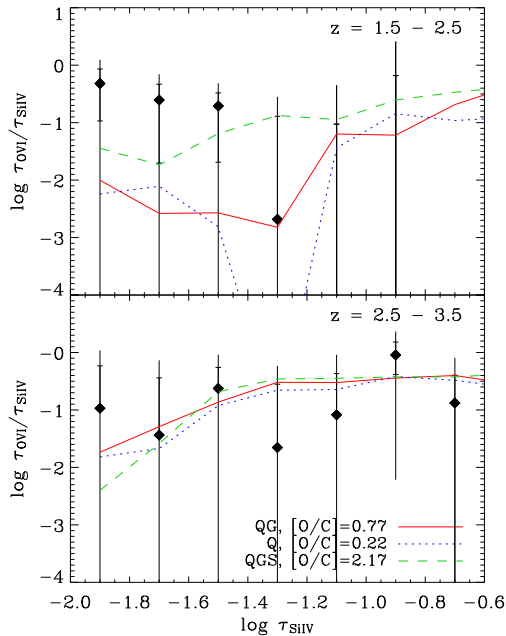


FIG. 10.— Rebinned median $\log \tau_{\text{OVI}}/\tau_{\text{SiIV}}$ vs. $\log \tau_{\text{SiIV}}$ in bins of z for the combined QSO sample. The two panels show bins centered at $z = 2$ and 3 with width $\Delta z = 1$. Data points are plotted with 1 and 2σ error bars. The lines represent corresponding simulation points (with errors suppressed and with $[\text{O}/\text{C}]$ chosen to minimize the χ^2) using different UVB models. The $\log \tau_{\text{SiIV}} = -1.35$ Q data point is set to the minimum allowed τ_{OVI} , $\log \tau_{\text{OVI}} = -6$.

lations – that contains O VI, but lacks H I and C IV. As suggested in §3.5 and Fig. 3, and further discussed below in §5.4, this might indicate the presence of a significant amount of collisionally ionized ($T > 10^5$ K) gas in the IGM.

4.3. τ_{OVI} versus τ_{SiIV} for the full sample

A third check on our measured $[\text{O}/\text{C}]$ is provided by the $\tau_{\text{OVI}}/\tau_{\text{SiIV}}$ ratio. Fig. 10 shows $\tau_{\text{OVI}}/\tau_{\text{SiIV}}$ versus τ_{SiIV} for our full sample, for two cuts in z . For each UVB the constant Si/C ratio derived in Paper III and the C distribution measured in Paper II are imposed on the simulations and the $[\text{O}/\text{C}]$ ratio is varied to minimize the χ^2 difference between the observed and simulated data points. Though the detection of $\tau_{\text{OVI}}/\tau_{\text{SiIV}}$ is weak, the simulations appear to adequately represent the observations in the redshift range where τ_{SiIV} is best detected, $2.5 \leq z \leq 3.5$. From these fits we infer, for this redshift interval, $[\text{O}/\text{C}]$ of 0.77 ± 0.19 , 0.24 ± 0.20 , and 2.17 ± 0.21 for UVB models QG, Q, and QGS, respectively; all are consistent with the results obtained from $\tau_{\text{OVI}}/\tau_{\text{CIV}}$, though all are somewhat higher. Because Si IV probes higher density gas than C IV (see Paper III), this again suggests that the simulations underpredict the amount of O VI in and near dense gas.

4.4. $[\text{O}/\text{H}]$ versus δ from $\tau_{\text{OVI}}/\tau_{\text{HI}}$ vs. τ_{HI}

As a final method, we can apply the “inversion method” developed in Paper II, to convert $\tau_{\text{OVI}}/\tau_{\text{HI}}$ vs. τ_{HI} into $[\text{O}/\text{H}]$ vs. δ by applying a density-dependent ionization correction. Then, using the measured distri-

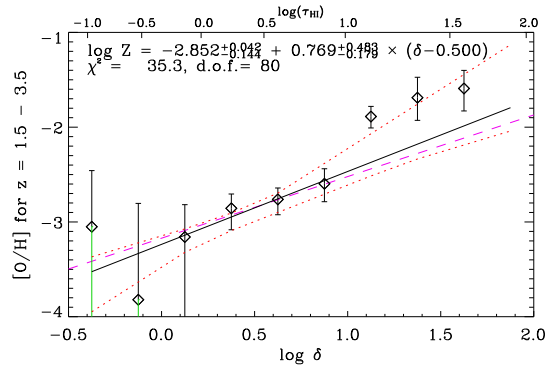


FIG. 11.— Median oxygen abundance vs. overdensity δ for $z=1.5$ – 3.5 . The inversion results for each QSO are binned in density bins of 0.125 dex. Data points are plotted with 1σ error bars, where green lines denote lower error of $-\infty$. The solid line indicates the least-squares fit to the individual data points for $\delta < 10$. Dotted curves represent the 1σ confidence limits, which were computed by bootstrap resampling the QSOs. The dashed line is the measured $[\text{O}/\text{H}]$ utilizing the derived $[\text{O}/\text{C}]$ results obtained from $\tau_{\text{OVI}}/\tau_{\text{CIV}}$ and assuming the $[\text{C}/\text{H}]$ distribution from Paper II.

bution of carbon from Paper II, an independent measurement of $[\text{O}/\text{C}]$ can be obtained.

In Figure 11 we show the derived $[\text{O}/\text{H}]$ versus δ for our preferred UVB model QG, with data from all z combined. The data points from the individual quasar spectra (an example is shown in Fig. 4) have been binned in density bins of 0.25 dex. The solid line shows the least-squares fit to the data points with $\delta < 10$ and the dotted curves indicate the 1σ confidence limits, with the resulting fit given in the upper left corner. The errors on the fits were determined by bootstrap resampling the QSOs. The dashed line is the value of $[\text{O}/\text{H}]$ given by the derived $[\text{O}/\text{C}] = 0.64$ result using $\tau_{\text{OVI}}/\tau_{\text{CIV}}$, and assuming a $[\text{C}/\text{H}]$ distribution from Paper II.

For $\delta < 10$, the $[\text{O}/\text{H}]$ derived from the ionization correction agrees very well with that determined from both $\tau_{\text{OVI}}/\tau_{\text{CIV}}$, and $\tau_{\text{OVI}}/\tau_{\text{HI}}$. This strengthens the result from §4.1 and §4.2 that $[\text{O}/\text{C}]$ is indeed constant for $-0.5 \leq \log \delta \leq 1$.

However, for $\delta > 10$ the ionization correction results in substantially more $[\text{O}/\text{H}]$ than that predicted using the previously-determined $[\text{C}/\text{H}]$ distribution and a fixed $[\text{O}/\text{C}]$ ratio. This is similar to the breakdown between the simulations and observed $\tau_{\text{OVI}}/\tau_{\text{HI}}$ seen in Fig. 8, and the erroneously high $[\text{O}/\text{H}]$ recovered for high- δ (see Fig. 5) when applying the ionization correction to the simulated spectra. Once again, this suggests the presence of collisionally ionized O VI.

4.5. Systematic uncertainties

The primary source of systematic uncertainty in, e.g. $[\text{O}/\text{C}]$ or $[\text{O}/\text{H}]$, is the complex modeling that must be performed to extract these values from the pixel correlations. The greatest combination of importance and uncertainty is clearly the uncertainty in the shape of the UVB; but this is discussed at length below in Sec. 5.1 so we here focus on other aspects of the modeling.

The good agreement between the four methods we have employed indicates that the method is sound; but it is also clear that there are real differences between the universe and our simulation. In particular, it is clear that

the real universe has an extra component of O VI at high density, almost certainly due to collisionally ionized gas that is not captured by those simulations. Nonetheless, if we exclude those high- τ_{HI} regions, the small discrepancies between [O/C] as measured using the different methods indicate that such effects probably do not contribute more than ~ 0.1 dex uncertainty to our basic results.

Another source of error that may be inaccurately assessed by our bootstrap resampling technique is that from continuum fitting. As shown in Table 1, our estimated rms error in the O VI absorption region is $\sim 1 - 4\%$. To test the effect of this error on our results, we have imposed an additional error on each observed spectrum on scales of 20, 80, and 320 Å, for a total added rms error of 2%, then recomputed our results. We find that our best fit [O/C] from τ_{OVI} versus τ_{CIV} , and from τ_{OVI} versus τ_{HI} , are both within ~ 0.03 dex. Further, both the individual binned points and linear fits of the [O/H] values computed from the full sample (Fig. 11) are all affected by this continuum error to a lesser degree than the quoted random errors. Thus, we conclude that the continuum fitting error is not a significant systematic affecting our results.

A final possible source of systematic error is that the O VI and C IV recombination rates used in the version of CLOUDY we have employed are too high by $\sim 50 - 75\%$ compared with recent experimental values, for the temperatures relevant to low-density photoionized gas. (Savin, *private communication*). For the range of densities $1 \lesssim \delta \lesssim 40$ we cover, this would imply a (density-dependent) correction of $0 - 0.1$ dex. This might change our overall fits by an amount comparable to the statistical errors, but is still much smaller than uncertainties stemming from the UVB shape, and cannot account for the 0.5 dex of excess in τ_{OVI} at high $\tau_{\text{HI}} \gtrsim 10$ shown in Fig. 11. Combining these possible sources, we estimate probable systematic errors of ~ 0.2 dex in our basic [O/C] and [O/H] values; this uncertainty may be somewhat greater in subsets of the data, particularly at high-density.

4.6. Densities and volume/mass fractions to which the results apply

It is important to emphasize that each quoted result is sensitive to, and applies to, only a certain range of gas densities. At the upper end, our results nominally concern gas of up to $\delta \sim 100$, though (as noted at length above) the high- τ_{HI} range of our data is likely to be affected by collisional ionization. That range is, however, not dominant: we have checked that if all pixels with $\tau_{\text{HI}} > 30$ are excluded from the analysis, the results given for [O/C] in columns 2 and 4 of Table 2 change only within the quoted errors.

The lower end of the gas density range probed is most straightforward in results from $\tau_{\text{OVI}}/\tau_{\text{HI}}$ (Figs. 8 and 11, which formally show OVI detections at 1σ using all QSOs at $z=2.5 - 3.5$ for $\log \tau_{\text{HI}} \gtrsim -0.1$, or $\log \delta \gtrsim 0.1$ and confident detections at $\log \delta \gtrsim 0.4$. In Paper III, the Si abundance results were sensitive to $\log \tau_{\text{HI}} \gtrsim 0.2$ ($\log \delta \gtrsim 0.2$), and in Paper II, C abundances were measured in much lower density gas. Thus our results provide indirect constraints on [O/C] and [O/Si] down to $\log \delta \sim 0.1 - 0.2$.

However, there are important caveats. First, the quoted results pertain to the the full density range

probed and thus are not necessarily very sensitive to the lowest densities. Second, because the pixel method only works if the element on the x-axis is more easily detectable than the element on the y-axis, direct measurements of [O/C] and [O/Si] from $\tau_{\text{OVI}}/\tau_{\text{CIV}}$ and $\tau_{\text{OVI}}/\tau_{\text{SiIV}}$ are dominated by much higher-density that gives $\tau_{\text{CIV}}, \tau_{\text{SiIV}} \gg -2.0$; thus while these results are consistent with our indirect constraints, they do not address the (somewhat implausible) possibility that at low densities O, Si, and C come from completely different gas phases. On the other hand, at *high* densities it is quite possible that OVI and SiIV emission are dominated by different phases, so the indirectly inferred [Si/O] values are probably both reliable and well-measured only in the moderate density range $\delta \sim 5 - 10$.

Although mass or volume filling-factors corresponding to these results are not well constrained (see, e.g., Schaye & Aguirre 2005), the forewarned reader can convert the density range $\delta \gtrsim 2$ correspond to into a volume using Paper II.

5. ANALYSIS AND DISCUSSION OF RESULTS

5.1. Relative abundances and the spectral shape of the UVB

The best fitting metallicities and corresponding $\chi^2/\text{d.o.f.}$ from Papers II, III and this work are shown in Table 2 for each UVB model. Two interesting results stand out. First, for all UVB models carbon is underabundant relative to both silicon and oxygen (being only marginally consistent with solar for UVB model Q). Second, all abundance ratios are sensitive to the UVB shape. A harder UVB results in a lower inferred [O/C] but a higher inferred [Si/C], making the [Si/O] ratio particularly sensitive to the spectral hardness of the UVB.

The extreme sensitivity of the inferred [Si/O] ratio to the spectral shape of the UV background makes it possible to constrain feasible UVB models by making only weak assumptions about the [Si/O] ratio. Since Si and O are both α elements, they are expected to trace each other relatively well. For example, using the nucleosynthetic yields of Portinari et al. (1998) and Marigo (2001) and a Chabrier (2003) initial mass function from $0.1 - 100 M_{\odot}$, the [Si/O] ratio of the ejecta of a population of age $t \gtrsim 10^8$ yr is predicted to be about 0.12 and -0.03 for stars of solar and 1 percent solar metallicity, respectively. This agrees well with observations of metal-poor stars, which find $[\text{Si}/\text{O}] \approx 0$ (Cayrel et al. 2004).

Tallying the results of this work with those of Papers II and III yields $[\text{Si}/\text{O}] = 0.11 \pm 0.08, 1.42 \pm 0.08,$ and -1.97 ± 0.1 for UVB models QG, Q, and QGS, respectively. Thus, our preferred model, QG, is nicely consistent with the expectations, but models Q and QG lead to inferred [Si/O] ratios that are highly inconsistent with both nucleosynthetic yields and observations of metal-poor stars. (Assuming $[\text{Si}/\text{C}] \simeq 0.5$ and $[\text{Si}/\text{O}] \simeq 0$ in the Q background, for example, raises the χ^2 of the fits in Figures 6 and 8 by 65 and 92, respectively; requiring this for QGS likewise raises the χ^2 by 138 and 81.) We conclude that the UVB has a spectral shape similar to that of model QG.

While our result using the QG UVB are broadly consistent with the abundance ratios in metal-poor stars and in yield calculations, the [O/C] and [Si/C] may be some-

what high, by $\sim 0.1 - 0.3$ dex. This is comparable to our systematic errors, but nevertheless interesting if taken seriously.

For example, the models of Nomoto et al. (2006) that include the contributions of hypernovae (defined as supernovae with kinetic energy $> 10\times$ that of normal core-collapse SNe) produce $[O/C] \approx 0.6$, and $[Si/C] \approx 0.65$, in agreement with our results.

5.2. Implications for cosmic abundances

In Paper II we combined the median $[C/H](\delta, z)$ with the width $\sigma([C/H](\delta, z))$ of the lognormal probability distribution of $[C/H]$ for $-0.5 \leq \log \delta \leq 2.0$ to determine the mean C abundance versus δ . This was then integrated over the mass-weighted probability distribution δ (obtained from our hydrodynamical simulation) to compute the contribution by gas in this density range to the overall mean cosmic $[C/H]$. Assuming that $[O/C]$ is *constant* over this density range⁹ we obtain, for our fiducial UVB model QG, $[O/H] = -2.14 \pm 0.14$, corresponding to

$$\Omega_{O,IGM} \simeq 3.3 \times 10^{-6} 10^{[O/H]+2.1} \left(\frac{\Omega_b}{0.045} \right). \quad (5)$$

Extrapolating our $[C/H]$ and $[O/C]$ results even further to the full density range of the simulation would yield values ≈ 0.2 dex higher but with more uncertainty, as we have argued that our results are unreliable at the highest densities.

Note that these results are relatively insensitive to the UVB (unlike those for $\Omega_{Si,IGM}$ in Paper III) because for a harder UVB, the inferred $[C/H]$ increases, while $[O/C]$ decreases. For our quasar-only model Q, these effects almost entirely cancel, yielding $[O/H] \approx -2.3$, and an $\Omega_{O,IGM}$ value 30% lower than for model QG. Note also that these estimates include the oxygen that resides in gas that is observable in C IV and O VI, but they do not include oxygen in intergalactic gas that is very hot ($T \gg 10^5$ K) or very cold ($T \ll 10^4$ K) and shielded from ionizing radiation.

If, following Bouche et al. (2007), we take $\Omega_{Z,IGM} = \Omega_{O,IGM}/0.6$, we then infer an intergalactic metal reservoir of $\Omega_{Z,IGM} \approx (4.3 - 6.8) \times 10^{-6}$. This can be compared to their estimate of the total $z \approx 2 - 3$ “metal budget” of $\Omega_Z \sim 2 - 3 \times 10^{-5}$, indicating that $\sim 15 - 35\%$ of metals produced prior to $z = 3$ reside in the component of the IGM that is studied here.

5.3. Previous Searches for Oxygen in the IGM

Previous studies have explored oxygen abundances in the IGM using both line-fitting (e.g., Rauch et al. 1997; Davé et al. 1998; Carswell et al. 2002; Bergeron et al. 2002; Simcoe et al. 2004; Bergeron & Herbert-Fort 2005) and pixel optical depths (Davé et al. 1998; Schaye et al. 2000a; Telfer et al. 2002; Aracil et al. 2004; Pieri & Haehnelt 2004).

Previous pixel studies did not attempt to convert their O VI detections into oxygen abundances; but we can compare to their recovered optical depths. Both Schaye et al. (2000a) and Aracil et al. (2004) claim detection of O VI down to $\tau_{HI} \approx 0.2$. Using our combined data

set binned in density (see Fig. 11), we obtain 1- σ detections down to about the mean density ($\tau_{HI} \approx 0.5$ at $z = 2.5$). While O VI is in principle an excellent tracer of metal in very low-density gas, in practice we find that for the higher redshifts where low densities are more easily probed, H I contamination is severe. Thus we are not in practice able to constrain metals in underdense gas as claimed in previous studies, in spite of a large sample and improved techniques of removing contaminants. On the high- τ_{HI} side, both Aracil et al. (2004) and Pieri & Haehnelt (2004) exclude pixels saturated in H I, so cannot probe $\log \tau_{HI} \gtrsim 0.5$. (This accounts, for example, for our detection of O VI in Q1422+230, while Pieri & Haehnelt (2004) had no detection in the same QSO). The study of Schaye et al. (2000a) did probe high τ_{HI} , where their results are broadly consistent with ours.

The studies of Carswell et al. (2002), Simcoe et al. (2004), Telfer et al. (2002), and Bergeron & Herbert-Fort (2005) did perform ionization corrections and we can compare our abundance determinations (relatively directly) to theirs. Carswell et al. (2002) assumed to abundance of oxygen relative to carbon to be solar and inferred metallicities for various UVB models and a number of O VI absorbers in $N_{HI} \sim 10^{15} \text{ cm}^{-2}$ systems at $z \approx 2$. They found that for relatively hard UV backgrounds, comparable to our model Q, the ionization models yielded densities in agreement with theoretical predictions for self-gravitating clouds with the observed H I column densities ($n_{HI} \sim 10^{-4} \text{ cm}^{-3}$; Schaye (2001)) and metallicities of $10^{-3} - 10^{-2}$ solar, in excellent agreement with our measurement of $[O/C] \approx [C/H] \approx -2.6$ for model Q at $z = 2$ and $\log \delta = 1.5$. We note that if Carswell et al. (2002) would have allowed oxygen to be overabundant relative to carbon, they would have found that softer UVB models are required to obtain density estimates that agree with theoretical expectations for gravitationally confined clouds.

Telfer et al. (2002) employed the Faint Object Spectrograph on *HST* to search for O V in QSO spectra from redshift $1.6 \leq z \leq 2.9$. The O VI/O V ratio found by the survey favored a UVB background similar to our Q, which they use to derive a metallicity of $-2.2 \lesssim [O/H] \lesssim -1.3$. While somewhat higher than our value, much of the difference may be attributable to their use of the 78th percentile in the O V/H I ratio. Assuming that $[O/H]$ has a scatter at fixed density similar to that in $[C/H]$ (see Paper (II)), this would correspond to a *median* of ~ 0.5 dex less, or $-2.7 \lesssim [O/H] \lesssim -1.8$, in fairly good agreement with our numbers.

Bergeron & Herbert-Fort (2005) divide their sample into “metal-poor absorbers” with $N(O\text{ VI})/N(H\text{ I}) < 0.25$, which they take to be predominantly photoionized, and “metal-rich absorbers” with $N(O\text{ VI})/N(H\text{ I}) > 0.25$, for which they assume a hotter phase. For the metal-poor systems they use a “hard” UVB and assume $[O/C] = 0$ to derive a range of $-3.0 \lesssim [O/H] \lesssim -1.0$, and for the metal-rich phase they infer a median $[O/H] \approx -0.80$ to -0.33 , depending upon the assumptions regarding the ionization balance. Combining their samples they estimate cosmic density $\Omega_{O,IGM} \approx (1.6 - 4.4) \times 10^{-6}$, corresponding to $-2.4 \lesssim [O/H] \lesssim -2.0$ if divided by the cosmic gas density $\Omega_b = 0.045$. While precise comparison is difficult, these numbers are consistent with our corresponding estimates of $[O/H] \approx -2.3$, or $\Omega_{O,IGM} \approx$

⁹ Note that this is an extrapolation beyond the range $2 \lesssim \delta \lesssim 10$ over which we have reliably *measured* Oxygen abundances.

3.3×10^{-6} using the Q UVB.

Simcoe et al. (2004) assume $[\text{O}/\text{C}]=0.5$ and 0.0 for UVB backgrounds comparable to our QG and Q, for $2.2 \lesssim z \lesssim 2.8$, so (as for the above studies) comparing derived $[\text{O}/\text{C}]$ values is less useful than several other points of comparison. First, in both backgrounds, their dependence of $[\text{O}/\text{H}]$ upon δ is similar to that found for $[\text{C}/\text{H}]$ vs. δ in Paper II, consistent with a constant $[\text{O}/\text{C}]$ value. Second, Simcoe et al. (2004) find that there is a clear jump in the median $[\text{O}/\text{H}]$ at $\delta \sim 10$, while a corresponding jump is not seen in $[\text{C}/\text{H}]$, similar to our results in §4.4. They also interpret this as possibly indicating that stronger absorbers are physically more complex or multiphased. Third, Simcoe et al. (2004) compute an overall contribution $\Omega_{\text{O,IGM}} \approx 1.0 \times 10^{-6}$, using their “hard” background; this would correspond to a cosmic average contribution of $[\text{O}/\text{H}] = -2.6$; these numbers are ≈ 0.3 dex lower than our values, but this should be regarded as good agreement given the number of assumptions made in each computation.

Finally, the studies of Rauch et al. (1997) Davé et al. (1998) are similar to ours in employing simulated spectra to attempt to match observed O VI absorption and thus constrain $[\text{O}/\text{C}]$ and $[\text{O}/\text{H}]$. Rauch et al. (1997) generated simulated spectra from a constant-metallicity simulation and compared ionic ratios to extant data, inferring $[\text{C}/\text{H}] \approx -2.5$ and evidence for overabundance of Si and O relative to carbon. Davé et al. (1998) used Q1422+230 and a quasar-only Haardt & Madau UVB model like ‘Q’. They found that their data is consistent with $[\text{O}/\text{C}] \approx 0$ and $[\text{C}/\text{H}] \approx -2.5$; these are quite consistent with our results using the Q UVB. As an alternative interpretation, they note that a softer UVB would give high $[\text{O}/\text{C}]$ (more characteristic of Type II supernova yields), but also lower $[\text{C}/\text{H}]$, again consistent with our findings; however they interpret this softness as due to patchy reionization, whereas we favor its explanation by the contribution of galaxies to the UVB.

5.4. Collisionally Ionized Gas

As discussed above, the difference between the inferred $[\text{O}/\text{H}]$ for $\delta \gtrsim 10$ and $\delta \lesssim 10$ is probably due to collisionally ionized gas, for reasons sketched in § 3.5. Fig. 3 shows that for $T \gg 10^5$ K, collisional ionization dominates and the optical depth ratios become independent of the density. For $T \ll 10^5$ K, on the other hand, the O VI/C IV and the O VI/H I ratios both drop rapidly with increasing density. Consequently, these ratios can be many orders of magnitude higher in hot, dense gas than in warm, dense gas. The lower the density, the smaller the differences become. In fact, at high densities the O VI fraction in warm gas is too small for O VI to be observable. Therefore, any O VI at the redshift of very strong H I absorption is likely to arise in a different phase than the associated H I and possibly even the associated C IV. The O VI phase must either have a much lower density or a much higher temperature.

Because the fraction of hot gas in our simulation is small at all densities, we effectively assume the gas to be photo-ionized when we compare with synthetic spectra and when we correct for ionization (as in Fig. 11). In the latter case, we also implicitly assume that O VI and H I absorption arise in the same gas phase.

Hence, our results from § 4.4 suggest the existence of

a detectable amount of O VI enriched hot ($T > 10^5$ K) gas associated with strong H I absorption. A possible physical explanation is that such O VI systems coincide with outer regions of high z galactic halos, where the effects of galactic winds may dominate the heating process. If the temperature exceeds 10^5 K in these regions, then this gas would contain significant O VI, while lacking C IV and H I. The latter two would then arise in a cooler gas phase, which has to be fairly dense in order to account for the strong H I absorption. The high density of the cooler phase implies that it would not produce significant photo-ionized O VI.

These results and inferences are consistent with other observational studies of O VI. Carswell et al. (2002) and Bergeron et al. (2002) both find that the majority of the detected absorption systems had temperatures determined from the line widths too low for collisional ionization, but cannot rule out higher temperatures for some absorbers. Indeed, the study of Simcoe et al. (2002) find their detected high-column density O VI lines associated with strong H I absorbers are broad enough to be consistent with collisional ionization. As noted above, Simcoe et al. (2004) find a jump in $[\text{O}/\text{H}]$ at $\delta \sim 10$ interpretable as a transition to a regime in which collisionally ionized gas affects the abundance inferences.

While collisionally ionized gas complicates oxygen abundance inferences, the flip-side is that O VI then provides an important probe of hot, enriched IG gas that is difficult to detect in C IV (e.g., Paper II). Indeed, hydrodynamical simulations by Theuns et al. (2002) and Oppenheimer & Davé (2006) predict that a significant portion of C IV is collisionally ionized. Hence, it would thus be very interesting to compare such simulations, employing O VI as a metallicity tracer, with the observations analyzed here.

6. CONCLUSIONS

We have studied the relative abundance of oxygen in the IGM by analyzing O VI, C IV, Si IV, and H I pixel optical depths derived from a set of high-quality VLT and Keck spectra of 17 QSOs at $2.1 \lesssim z \lesssim 3.6$, and we have compared them to realistic, synthetic spectra drawn from a hydrodynamical simulation to which metals have been added. Our fiducial model employs the ionizing background model (“QG”) taken from Haardt & Madau (2001) for quasars and galaxies (rescaled to reproduce the observed mean Ly α absorption). The simulation assumes a silicon abundance as calculated in Paper III, $[\text{Si}/\text{C}] = 0.77 \pm 0.05$, and a carbon abundance as derived in Paper II: at a given overdensity δ and redshift z , $[\text{C}/\text{H}]$ has a lognormal probability distribution centered on $-3.47 + 0.65(\log \delta - 0.5)$ and of width 0.70 dex. The main conclusions from this analysis are as follows:

- For $1.9 \leq z \leq 3.6$, $\tau_{\text{HI}} \leq 10$, and $\delta \leq 10$ (when smoothed on the scale of the H I absorption, $10 - 10^2$ kpc), the fiducial simulation utilized in Papers I, II, and III consistently agrees with the observed $\tau_{\text{OVI}}/\tau_{\text{CIV}}(\tau_{\text{CIV}})$, $\tau_{\text{OVI}}/\tau_{\text{HI}}(\tau_{\text{HI}})$, and (to a lesser degree) $\tau_{\text{OVI}}/\tau_{\text{SiIV}}(\tau_{\text{SiIV}})$. Fitting $\tau_{\text{OVI}}/\tau_{\text{CIV}}(\tau_{\text{CIV}})$ yields a constant $[\text{O}/\text{C}] = 0.66 \pm 0.06$, with estimated systematic errors within ± 0.2 dex. Converting the observed $\tau_{\text{OVI}}/\tau_{\text{HI}}(\tau_{\text{HI}})$ into $[\text{O}/\text{C}](\delta)$ using the ionization correction method of Paper II

further supports these results.

- The relative abundances $[O/C]$ and (especially) $[O/Si]$ are sensitive to the UVB shape. We find that our fiducial (Haardt & Madau 2001, quasars and galaxies) spectrum gives reasonable results for both, but that significantly softer or harder UVBs, such as the Haardt & Madau 2001 quasar-only UVB, give results that are highly inconsistent with both theoretical yields and observed abundance ratios in other low-metallicity environments, and should not be considered tenable.
- Our results, both from applying the ionization correction and from comparing the simulations to the observations, suggest no evolution in $[O/H]$ over the redshift range $1.9 \lesssim z \lesssim 3.6$, but a strong dependence on δ . Both results are consistent with those found in Paper II for $[C/H]$.
- For $\tau_{HI} \geq 10$ and $\delta \geq 10$ the value of $[O/C]$ (derived by comparison to the simulations) is inconsistent with that found at lower densities, and ~ 0.5 dex higher than that predicted using the carbon distribution of Paper II and a density-independent $[O/C]$ value. This might in principle suggest a density-dependent $[O/C]$ ratio, but we favor the interpreta-

tion that a fraction of the high- δ O VI absorbing gas is collisionally ionized, and that this leads to an erroneously large ionization correction in this regime. This interpretation is supported by our simulated spectra as well as by the observation that O VI lines associated with strong H I absorbers tend to be broader than those associated with weak H I systems (Carswell et al. 2002; Simcoe et al. 2002; Bergeron et al. 2002).

We are grateful to Wallace Sargent, Michael Rauch and Tae-Sun Kim for providing the Keck/HIRES and VLT/UVES data used here and in Papers I-III. We are also extremely grateful to Daniel Savin for his assistance in understanding and assessing the systematic uncertainties in recombination rates. Thanks also to Rob Wiersma for computing the expected Si/O ratio from nucleosynthetic yields taken from the literature. We thank the anonymous referee for providing comprehensive and helpful feedback that improved the manuscript. AA and CDH gratefully acknowledge support from NSF Grant AST-0507117 and JS from Marie Curie Excellence Grant MEXT-CT-2004-014112.

REFERENCES

- Aguirre, A., Schaye, J., & Theuns, T. 2002, *ApJ*, 576, 1 (Paper I)
Aguirre, A., Schaye, J., Kim, T., Theuns, T., Rauch, M., & Sargent, W.L.W. 2004, *ApJ*, 602, 38 (Paper III)
Anders, E. & Grevesse, N. 1989, *Geochim. Cosmochim. Acta*, 53, 197
Aracil, B., Petitjean, P., Pichon, C., & Bergeron, J. 2004, *A&A*, 419, 811
Bergeron, J., Aracil, B., Petitjean, P., & Pichon, C. 2002, *A&A*, 396, L11
Bergeron, J. & Herbert-For, S. 2005, *astro-ph/0506700*
Bouche, N., Lehnert, M., Aguirre, A., Péroux, C., & Bergeron, J. 2007, *MNRAS*, submitted.
Carswell, B., Schaye, J., & Tae-Sun, K. 2002, *ApJ*, 578, 43
Cayrel, R. et al. 2004, *A&A*, 416, 1117
Chabrier, G. 2003, *PASP*, 115, 763
D’Odorico, S., Cristiani, S., Dekker, H., Hill, V., Kaufer, A., Kim, T., & Primas, F. 2000, *Proc. SPIE*, 4005, 121
Davé, R., Hellsten, U., Hernquist, L., Katz, N., & Weinberg, D. H. 1998, *ApJ*, 509, 661
Erb, D. K., Shapley, A. E., Pettini, M., Steidel, C. C., Reddy, N. A., & Adelberger, K. L. 2006, *ApJ*, 644, 813
Ferland, G. J. 2000, *Revista Mexicana de Astronomia y Astrofisica Conference Series*, 9, 153
Ferland, G. J., Korista, K. T., Verner, D. A., Ferguson, J. W., Kingdon, J. B., & Verner, E. M. 1998, *PASP*, 110, 761
Haardt, F. & Madau, P. 2001, to be published in the proceedings of XXXVI Rencontres de Moriond, *astro-ph/0106018*
Kauffmann, G., White, S. D. M., & Guiderdoni, B. 1993, *MNRAS*, 264, 201
Kim, T.-S., Cristiani, S., & D’Odorico, S. 2001, *A&A*, 373, 757
Kim, T.-S., Cristiani, S., & D’Odorico, S. 2002, *A&A*, 383, 747
Kim, T.-S., Viel, M., Haehnelt, M. G., Carswell, R. F., & Cristiani, S. 2004, *MNRAS*, 347, 355
Marigo, P. 2001, *A&A*, 370, 194
Nomoto, K., Tominaga, N., Umeda, H., Kobayashi, C., & Maeda, K. 2006, *MNRAS*, submitted; *astro-ph/0605725*
Oppenheimer, B. D., & Davé, R. 2006, *MNRAS*, 373, 1265
Pieri, M., & Haehnelt, M. 2004, *MNRAS*, 347, 985
Pettini, M., Madau, P., Bolte, M., Prochaska, J. X., Ellison, S. L., & Fan, X. 2003, *ApJ*, 594, 695
Portinari, L., Chiosi, C., & Bressan, A. 1998, *A&A*, 334, 505
Rauch, M., Haehnelt, M. G., & Steinmetz, M. 1997, *ApJ*, 481, 601
Ryan-Weber, E. V., Pettini, M., & Madau, P. 2006, *MNRAS*, 371, L78
Savin, D. W. 2000, *ApJ*, 533, 106
Schaye, J. 2001, *ApJ*, 559, 507
Schaye, J., & Aguirre, A. 2005, in *From Lithium to Uranium: Elemental Tracers of Early Cosmic Evolution*, 228, 557
Schaye, J., Rauch, M., Sargent, W. L. W., & Kim, T. 2000a, *ApJ*, 541, L1
Schaye, J., Theuns, T., Rauch, M., Efstathiou, G., & Sargent, W. L. W. 2000b, *MNRAS*, 318, 817
Schaye, J., Aguirre, A., Kim, T.-S., Theuns, T., Rauch, M., & Sargent, W. L. W. 2003, *ApJ*, 596, 768 (Paper II)
Schaye, J., Carswell, R. F., & Kim, T.-S. 2007, *MNRAS*, 379, 1169
Simcoe, R.A., Sargent, W.L.W., Rauch, M. 2002, *ApJ*, 578, 737
Simcoe, R.A., Sargent, W.L.W., Rauch, M. 2004, *ApJ*, 606, 92
Simcoe, R. A. 2006, *ApJ*, 653, 977
Somerville, R. S., & Primack, J. R. 1999, *MNRAS*, 310, 1087
Songaila, A. 2001, *ApJ*, 561, L153
Springel, V., & Hernquist, L. 2003, *MNRAS*, 339, 312
Telfer, R.C., Kriss, G.A., Zheng, W., Davidsen, A.F., Tytler, D. 2002, *ApJ*, 579, 500
Theuns, T., Viel, M., Kay, S., Schaye, J., Carswell, R. F., & Tzanavaris, P. 2002, *ApJ*, 578, L5
Tremonti, C. A., et al. 2004, *ApJ*, 613, 898
Vogt, S. S. et al. 1994, *Proc. SPIE*, 2198, 362